UNIVERSITY OF AMSTERDAM

UvA-DARE (Digital Academic Repository)

The 2012 Flare of PG 1553+113 Seen with H.E.S.S. and Fermi-LAT

Abramowski, A.; et al., [Unknown]; Balzer, A.; Berge, D.; Bryan, M.; Salek, D.; Vink, J.

DOI
10.1088/0004-637X/802/1/65

Publication date
2015

Document Version
Final published version

Published in
Astrophysical Journal

Link to publication

Citation for published version (APA):
Abramowski, A., et al., U., Balzer, A., Berge, D., Bryan, M., Salek, D., & Vink, J. (2015). The 2012 Flare of PG 1553+113 Seen with H.E.S.S. and Fermi-LAT. *Astrophysical Journal*, *802*(1), Article 65. https://doi.org/10.1088/0004-637X/802/1/65

General rights
It is not permitted to download or to forward/distribute the text or part of it without the consent of the author(s) and/or copyright holder(s), other than for strictly personal, individual use, unless the work is under an open content license (like Creative Commons).

Disclaimer/Complaints regulations
If you believe that digital publication of certain material infringes any of your rights or (privacy) interests, please let the Library know, stating your reasons. In case of a legitimate complaint, the Library will make the material inaccessible and/or remove it from the website. Please Ask the Library: https://uba.uva.nl/en/contact, or a letter to: Library of the University of Amsterdam, Secretariat, P.O. Box 19185, 1000 GD Amsterdam, The Netherlands. You will be contacted as soon as possible.

UvA-DARE is a service provided by the library of the University of Amsterdam (https://dare.uva.nl)

Download date:07 Oct 2026

The Astrophysical Journal, 802:65 (14pp), 2015 March 20 doi:10.1088/0004-637X/802/1/65
© 2015. The American Astronomical Society. All rights reserved.

THE 2012 FLARE OF PG 1553+113 SEEN WITH H.E.S.S. AND *FERMI*-LAT

A. Abramowski[1], F. Aharonian[2,3,4], F. Ait Benkhali[2], A. G. Akhperjanian[4,5], E. O. Angüner[6], M. Backes[7], S. Balenderan[8], A. Balzer[9], A. Barnacka[10,11], Y. Becherini[12], J. Becker Tjus[13], D. Berge[14], S. Bernhard[15], K. Bernlöhr[2,6], E. Birsin[6], J. Biteau[16,17], M. Böttcher[18], C. Boisson[19], J. Bolmont[20], P. Bordas[21], J. Bregeon[22], F. Brun[23], P. Brun[23], M. Bryan[9], T. Bulik[24], S. Carrigan[2], S. Casanova[2,25], P. M. Chadwick[8], N. Chakraborty[2], R. Chalme-Calvet[20], R. C. G. Chaves[22], M. Chrétien[20], S. Colafrancesco[26], G. Cologna[27], J. Conrad[28,43], C. Couturier[20], Y. Cui[21], M. Dalton[29,44], I. D. Davids[7,18], B. Degrange[16], C. Deil[2], P. deWilt[30], A. Djannati-Ataï[31], W. Domainko[2], A. Donath[2], L. O'C. Drury[3], G. Dubus[32], K. Dutson[33], J. Dyks[34], M. Dyrda[25], T. Edwards[2], K. Egberts[35], P. Eger[2], P. Espigat[31], C. Farnier[28], S. Fegan[16], F. Feinstein[22], M. V. Fernandes[1], D. Fernandez[22], A. Fiasson[36], G. Fontaine[16], A. Förster[2], M. FüSSling[35], S. Gabici[31], M. Gajdus[6], Y. A. Gallant[22], T. Garrigoux[20], G. Giavitto[37], B. Giebels[16], J. F. Glicenstein[23], D. Gottschall[21], M.-H. Grondin[2,27], M. Grudzińska[24], D. Hadsch[15], S. Häffner[38], J. Hahn[2], J. Harris[8], G. Heinzelmann[1], G. Henri[32], G. Hermann[2], O. Hervet[19], A. Hillert[2], J. A. Hinton[33], W. Hofmann[2], P. Hofverberg[2], M. Holler[35], D. Horns[1], A. Ivascenko[18], A. Jacholkowska[20], C. Jahn[38], M. Jamrozy[10], M. Janiak[34], F. Jankowsky[27], I. Jung[38], M. A. Kastendieck[1], K. Katarzyński[39], U. Katz[38], S. Kaufmann[27], B. Khélifi[31], M. Kieffer[20], S. Klepser[37], D. Klochkov[21], W. Kluźniak[34], D. Kolitzus[15], Nu. Komin[26], K. Kosack[23], S. Krakau[13], F. Krayzel[36], P. P. Krüger[18], H. Laffon[29], G. Lamanna[36], J. Lefaucheur[31], V. Lefranc[23], A. Lemiére[31], M. Lemoine-Goumard[29], J.-P. Lenain[20], T. Lohse[6], A. Lopatin[38], C.-C. Lu[2], V. Marandon[2], A. Marcowith[22], R. Marx[2], G. Maurin[36], N. Maxted[30], M. Mayer[35], T. J. L. McComb[8], J. Méhault[29,44], P. J. Meintjes[40], U. Menzler[13], M. Meyer[28], A. M. W. Mitchell[2], R. Moderski[34], M. Mohamed[27], K. Morå[28], E. Moulin[23], T. Murach[6], M. de Naurois[16], J. Niemiec[25], S. J. Nolan[8], L. Oakes[6], H. Odaka[2], S. Ohm[37], B. Opitz[1], M. Ostrowski[10], I. Oya[6], M. Panter[2], R. D. Parsons[2], M. Paz Arribas[6], N. W. Pekeur[18], G. Pelletier[32], J. Perez[15], P.-O. Petrucci[32], B. Peyaud[23], S. Pita[31], H. Poon[2], G. Pühlhofer[21], M. Punch[31], A. Quirrenbach[27], S. Raab[38], I. Reichardt[31], A. Reimer[15], O. Reimer[15], M. Renaud[22], R. de los Reyes[2], F. Rieger[2], L. Rob[41], C. Romoli[3], S. Rosier-Lees[36], G. Rowell[30], B. Rudak[34], C. B. Rulten[19], V. Sahakian[4,5], D. Salek[42], D. A. Sanchez[36], A. Santangelo[21], R. Schlickeiser[13], F. Schüssler[23], A. Schulz[37], U. Schwanke[6], S. Schwarzburg[21], S. Schwemmer[27], H. Sol[19], F. Spanier[18], G. Spengler[28], F. Spies[1], Ł. Stawarz[10], R. Steenkamp[7], C. Stegmann[35,37], F. Stinzing[38], K. Stycz[37], I. Sushch[6,18], J.-P. Tavernet[20], T. Tavernier[31], A. M. Taylor[3], R. Terrier[31], M. Tluczykont[1], C. Trichard[36], K. Valerius[38], C. van Eldik[38], B. van Soelen[40], G. Vasileiadis[22], J. Veh[38], C. Venter[18], A. Viana[2], P. Vincent[20], J. Vink[9], H. J. Völk[2], F. Volpe[2], M. Vorster[18], T. Vuillaume[32], P. Wagner[6], R. M. Wagner[28], M. Ward[8], M. Weidinger[13], Q. Weitzel[2], R. White[33], A. Wierzcholska[25], P. Willmann[38], A. Wörnlein[38], D. Wouters[23], R. Yang[2], V. Zabalza[2,33], D. Zaborov[16], M. Zacharias[27], A. A. Zdziarski[34], A. Zech[19], and H.-S. Zechlin[1]

(H.E.S.S. Collaboration)

[1] Universität Hamburg, Institut für Experimentalphysik, Luruper Chaussee 149, D-22761 Hamburg, Germany
[2] Max-Planck-Institut für Kernphysik, P.O. Box 103980, D-69029 Heidelberg, Germany
[3] Dublin Institute for Advanced Studies, 31 Fitzwilliam Place, Dublin 2, Ireland
[4] National Academy of Sciences of the Republic of Armenia, Marshall Baghramian Avenue, 24, 0019 Yerevan, Republic of Armenia
[5] Yerevan Physics Institute, 2 Alikhanian Brothers St., 375036 Yerevan, Republic of Armenia
[6] Institut für Physik, Humboldt-Universität zu Berlin, Newtonstr. 15, D-12489 Berlin, Germany
[7] University of Namibia, Department of Physics, Private Bag 13301, Windhoek, Namibia
[8] University of Durham, Department of Physics, South Road, Durham DH1 3LE, UK
[9] GRAPPA, Anton Pannekoek Institute for Astronomy, University of Amsterdam, Science Park 904, 1098 XH Amsterdam, The Netherlands
[10] Obserwatorium Astronomiczne, Uniwersytet Jagielloński, ul. Orla 171, 30-244 Kraków, Poland
[11] now at Harvard-Smithsonian Center for Astrophysics, 60 Garden St, MS-20, Cambridge, MA 02138, USA
[12] Department of Physics and Electrical Engineering, Linnaeus University, SE-351 95 Växjö, Sweden
[13] Institut für Theoretische Physik, Lehrstuhl IV: Weltraum und Astrophysik, Ruhr-Universität Bochum, D-44780 Bochum, Germany
[14] GRAPPA, Anton Pannekoek Institute for Astronomy and Institute of High-Energy Physics, University of Amsterdam, Science Park 904, 1098 XH Amsterdam, The Netherlands
[15] Institut für Astro- und Teilchenphysik, Leopold-Franzens-Universität Innsbruck, A-6020 Innsbruck, Austria
[16] Laboratoire Leprince-Ringuet, Ecole Polytechnique, CNRS/IN2P3, F-91128 Palaiseau, France
[17] now at Santa Cruz Institute for Particle Physics, Department of Physics, University of California at Santa Cruz, Santa Cruz, CA 95064, USA
[18] Centre for Space Research, North-West University, Potchefstroom 2520, South Africa
[19] LUTH, Observatoire de Paris, CNRS, Université Paris Diderot, 5 Place Jules Janssen, F-92190 Meudon, France
[20] LPNHE, Université Pierre et Marie Curie Paris 6, Université Denis Diderot Paris 7, CNRS/IN2P3, 4 Place Jussieu, F-75252, Paris Cedex 5, France; camille.couturier@lpnhe.in2p3.fr, jlenain@lpnhe.in2p3.fr
[21] Institut für Astronomie und Astrophysik, Universität Tübingen, Sand 1, D-72076 Tübingen, Germany
[22] Laboratoire Univers et Particules de Montpellier, Université Montpellier 2, CNRS/IN2P3, CC 72, Place Eugène Bataillon, F-34095 Montpellier Cedex 5, France
[23] DSM/Irfu, CEA Saclay, F-91191 Gif-Sur-Yvette Cedex, France; francois.brun@cea.fr
[24] Astronomical Observatory, The University of Warsaw, Al. Ujazdowskie 4, 00-478 Warsaw, Poland
[25] Instytut Fizyki Jądrowej PAN, ul. Radzikowskiego 152, 31-342 Kraków, Poland
[26] School of Physics, University of the Witwatersrand, 1 Jan Smuts Avenue, Braamfontein, Johannesburg, 2050, South Africa
[27] Landessternwarte, Universität Heidelberg, Königstuhl, D-69117 Heidelberg, Germany
[28] Oskar Klein Centre, Department of Physics, Stockholm University, Albanova University Center, SE-10691 Stockholm, Sweden
[29] Université Bordeaux 1, CNRS/IN2P3, Centre d'Études Nucléaires de Bordeaux Gradignan, F-33175 Gradignan, France
[30] School of Chemistry & Physics, University of Adelaide, Adelaide 5005, Australia

[31] APC, AstroParticule et Cosmologie, Université Paris Diderot, CNRS/IN2P3, CEA/Irfu, Observatoire de Paris, Sorbonne Paris Cité, 10, rue Alice Domon et Léonie Duquet, F-75205 Paris Cedex 13, France; julien.lefaucheur@apc.univ-paris7.fr
[32] Univ. Grenoble Alpes, IPAG, F-38000 Grenoble, France CNRS, IPAG, F-38000 Grenoble, France
[33] Department of Physics and Astronomy, The University of Leicester, University Road, Leicester, LE1 7RH, UK
[34] Nicolaus Copernicus Astronomical Center, ul. Bartycka 18, 00-716 Warsaw, Poland
[35] Institut für Physik und Astronomie, Universität Potsdam, Karl-Liebknecht-Strasse 24/25, D-14476 Potsdam, Germany
[36] Laboratoire d'Annecy-le-Vieux de Physique des Particules, Université de Savoie, CNRS/IN2P3, F-74941 Annecy-le-Vieux, France; david.sanchez@lapp.in2p3.fr
[37] DESY, D-15738 Zeuthen, Germany
[38] Universität Erlangen-Nürnberg, Physikalisches Institut, Erwin-Rommel-Str. 1, D-91058 Erlangen, Germany
[39] Centre for Astronomy, Faculty of Physics, Astronomy and Informatics, Nicolaus Copernicus University, Grudziadzka 5, 87-100 Torun, Poland
[40] Department of Physics, University of the Free State, P.O. Box 339, Bloemfontein 9300, South Africa
[41] Charles University, Faculty of Mathematics and Physics, Institute of Particle and Nuclear Physics, V Holešovičkách 2, 180 00 Prague 8, Czech Republic
[42] GRAPPA, Institute of High-Energy Physics, University of Amsterdam, Science Park 904, 1098 XH Amsterdam, The Netherlands
Received 2014 December 17; accepted 2015 January 11; published 2015 March 24

ABSTRACT

Very high energy (VHE, $E > 100$ GeV) γ-ray flaring activity of the high-frequency peaked BL Lac object PG 1553+113 has been detected by the H.E.S.S. telescopes. The flux of the source increased by a factor of 3 during the nights of 2012 April 26 and 27 with respect to the archival measurements with a hint of intra-night variability. No counterpart of this event has been detected in the *Fermi*-Large Area Telescope data. This pattern is consistent with VHE γ-ray flaring being caused by the injection of ultrarelativistic particles, emitting γ-rays at the highest energies. The dataset offers a unique opportunity to constrain the redshift of this source at $z = 0.49 \pm 0.04$ using a novel method based on Bayesian statistics. The indication of intra-night variability is used to introduce a novel method to probe for a possible Lorentz invariance violation (LIV), and to set limits on the energy scale at which Quantum Gravity (QG) effects causing LIV may arise. For the subluminal case, the derived limits are $E_{\mathrm{QG},1} > 4.10 \times 10^{17}$ GeV and $E_{\mathrm{QG},2} > 2.10 \times 10^{10}$ GeV for linear and quadratic LIV effects, respectively.

Key words: BL Lacertae objects: individual (PG 1553+113) – galaxies: active – galaxies: distances and redshifts – gamma-rays: galaxies

1. INTRODUCTION

Blazars are active galactic nuclei (AGNs) with their jets closely aligned with the line of sight to the Earth (Urry & Padovani 1995). Among their particularities is flux variability at all wavelengths on various time scales, from years down to (in some cases) minutes (Gaidos et al. 1996; Aharonian et al. 2007a). Flaring activity of blazars is of great interest for probing the source-intrinsic physics of relativistic jets, relativistic particle acceleration and generation of high-energy radiation, as well as for conducting fundamental physics tests. On the one hand, exploring possible spectral variability between flaring and stationary states helps to understand the electromagnetic emission mechanisms at play in the jet. On the other hand, measuring the possible correlation between photon energies and arrival times allows one to test for possible Lorentz invariance violation (LIV) leading to photon-energy-dependent variations in the speed of light in vacuum.

Located in the Serpens Caput constellation, PG 1553+113 was discovered by Green et al. (1986), who first classified it as a BL Lac object. Later the classification was refined to a high-frequency peaked BL Lac object (HBL, Giommi et al. 1995). PG 1553+113 exhibits a high X-ray to radio flux ($\log (F_{2\,\mathrm{keV}}/F_{5\,\mathrm{GHz}}) > -4.5$, Osterman et al. 2006), which places it among the most extreme HBLs (Rector et al. 2003). The object was observed in X-rays by multiple instruments in different flux states. Its 2–10 keV energy flux ranges from 0.3×10^{-11} erg cm^{-2} s^{-1} (Osterman et al. 2006) to 3.5×10^{-11} erg cm^{-2} s^{-1} (Reimer et al. 2008) but no fast variability (in the sub-hour time scale) has been detected so far.

PG 1553+113 was discovered at very high energies (VHE, $E > 100$ GeV) by H.E.S.S. (Aharonian et al. 2006a, 2008) with a photon index of $\Gamma = 4.0 \pm 0.6$. At high energies (HE, 100 MeV $< E <$ 300 GeV) the source has been detected by the *Fermi* Large Area Telescope (LAT) (Abdo et al. 2009b, 2010a) with a very hard photon index of $\Gamma = 1.68 \pm 0.03$, making this object the one with the largest HE–VHE spectral break ($\Delta\Gamma \approx 2.3$) ever measured. No variability in *Fermi*-LAT was found by Abdo et al. (2009b, 2010a) on daily or weekly time scales, but using an extended data set of 17 months, Aleksić et al. (2012) reported variability above 1 GeV with flux variations of a factor of ~5 on a yearly time scale.

With 5 yr of monitoring data of the MAGIC telescopes, Aleksić et al. (2012) discovered variability in VHE γ-rays with only modest flux variations (from 4% to 11% of the Crab Nebula flux). In addition to the high X-ray variability, this behavior can be interpreted as evidence for Klein–Nishina effects (Abdo et al. 2010a) in the framework of a synchrotron self-Compton model. The source underwent VHE γ-ray flares in 2012 March (Cortina 2012a) and April (Cortina 2012b), detected by the MAGIC telescopes. During the March flare, the source was at a flux level of about 15% of that of the Crab Nebula, while in April it reached ≈50%. During those VHE γ-ray flares, also a brightening in X-ray, UV and optical wavelengths has been noticed by the MAGIC collaboration. A detailed study of the MAGIC telescopes and multi-wavelength data is in press (Aleksić et al. 2014). The latter event triggered the H.E.S.S. observations reported in this work. Note that the VERITAS collaboration has reported an overall higher flux in 2012 (Aliu et al. 2015) in VHE.

Despite several attempts to measure it, the redshift of PG 1553+113 still suffers from uncertainties. Different attempts, including optical spectroscopy (Treves et al. 2007; Aharonian et al. 2008) or comparisons of the HE and VHE spectra of PG 1553+113 (Prandini et al. 2009; Sanchez

[43] Wallenberg Academy Fellow.
[44] Funded by contract ERC-StG-259391 from the European Community.

Table 1
Summary of the Statistics for Both Data Sets (First Column)

Data Set	ON	OFF	r	Excess	Significance	$E_{\rm th}$ (GeV)	Zenith Angle	$P_{\chi^2}^{\rm cst}$
Pre-flare	2205	13033	0.100	901.7	21.5	217	34°	0.77
Flare	559	1593	0.105	391.2	22.0	240	52°	3.3×10^{-3}

Note. The second and third columns give the number of ON and OFF events. The fourth column gives the ratio between ON and OFF exposures (r). The excess and the corresponding significance are given, as well as the energy threshold and the mean zenith angle of the source during the observations. The last column presents the probability of the flux to be constant within the observations (see text).

Table 2
Summary of the Fitted Spectral Parameters for the Pre-flare and the Flare Data Sets and the Corresponding Integral Flux I Calculated Above 300 GeV

Data Set (Model)	Spectral Parameters	I ($E > 300$ GeV) (10^{-12} ph cm^{-2} s^{-1})	$E_{\rm dec}$ (GeV)
Pre-flare (PWL)	$\Gamma = 4.8 \pm 0.2_{\rm stat} \pm 0.2_{\rm sys}$	$4.4 \pm 0.4_{\rm stat} \pm 0.9_{\rm sys}$	306
Pre-flare (LP)	$a = 5.4 \pm 0.4_{\rm stat} \pm 0.1_{\rm sys}$ $b = 4.0 \pm 1.4_{\rm stat} \pm 0.2_{\rm sys}$	$5.0 \pm 0.6_{\rm stat} \pm 1.0_{\rm sys}$	...
Flare (PWL)	$\Gamma = 4.9 \pm 0.3_{\rm stat} \pm 0.2_{\rm sys}$	$15.1 \pm 1.3_{\rm stat} \pm 3.0_{\rm sys}$	327

Note. The Last Column gives the Decorrelation Energy.

et al. 2013), were made. Based on the assumption that the extragalactic background light (EBL)-corrected VHE spectral index is equal to the *Fermi*-LAT one, Prandini et al. (2009) derived an upper limit (UL) of $z < 0.67$. Comparing PG 1553+113 statistically with other known VHE emitters and taking into account a possible intrinsic γ-ray spectral break through a simple emission model, Sanchez et al. (2013) constrained the redshift to be below 0.64 and Aliu et al. (2015) constrained it at $z < 0.62$ using VHE data only. The best estimate to-date was obtained by Danforth et al. (2010) who found the redshift to be between 0.43 and 0.58 using far-ultraviolet spectroscopy.

This paper concentrates on the HE and VHE emission of PG 1553+113 and is divided as follows: Sections 2.1 and 2.2 present the H.E.S.S. and *Fermi*-LAT analyses. The discussion, in Section 3, includes the determination of the redshift using a novel method and the constraints derived on LIV using a modified likelihood formulation. Throughout this paper a ΛCDM cosmology with $H_0 = 70.4 \pm 1.4$ km s^{-1}Mpc^{-1}, $\Omega_m = 0.27 \pm 0.03$, $\Omega_\Lambda = 0.73 \pm 0.03$ from *WMAP* (Komatsu et al. 2011) is assumed.

2. DATA ANALYSIS

2.1. H.E.S.S. Observations and Analysis

H.E.S.S. is an array of five imaging atmospheric Cherenkov telescopes located in the Khomas highland in Namibia (23°16′18″ S, 16°30′01″ E), at an altitude of 1800 m above sea level (Hinton & the H.E.S.S. Collaboration 2004). The fifth H.E.S.S. telescope was added to the system in 2012 July and is not used in this work, reporting only on observations prior to that time.

PG 1553+113 was observed with H.E.S.S. in 2005 and 2006 (Aharonian et al. 2008). No variability was found in these observations, which will be referred to as the "pre-flare" data set in the following. New observations were carried out in 2012 April after flaring activity at VHE was reported by the MAGIC collaboration ("flare" data set, Cortina 2012b).

The pre-flare data set is composed of 26.4 live time hours of good-quality data (Aharonian et al. 2006b). For the flare period, eight runs of ∼28 minutes each were taken during the nights of 2012 April 26 and 27, corresponding to 3.5 hr of live time. All the data were taken in wobble mode, for which the source is observed with an offset of 0.°5 with respect to the center of the instrument's field of view, yielding an acceptance-corrected live time of 24.7 and 3.2 hr for the pre-flare and flare data sets, respectively.

Data were analyzed using the `Model` analysis (de Naurois & Rolland 2009) with `Loose cuts`. This method–based on the comparison of detected shower images with a pre-calculated model–achieves a better rejection of hadronic air showers and a better sensitivity at lower energies than analysis methods based on Hillas parameters. The chosen cuts, best suited for sources with steep spectra such as PG 1553+113,[45] require a minimum image charge of 40 photoelectrons, which provides an energy threshold of ∼217 GeV for the pre-flare and ∼240 GeV for the flare data set.[46] All the results presented in this paper were cross-checked with the independent analysis chain described in Becherini et al. (2011).

Events in a circular region (ON region) centered on the radio position of the source, $\alpha_{\rm J2000} = 15^{\rm h}55^{\rm m}43\overset{\rm s}{.}04$, $\delta_{\rm J2000} = 11°11'24\overset{''}{.}4$ (Green et al. 1986), with a maximum squared angular distance of 0.0125 deg^2, are used for the analysis. In order to estimate the background in this region, the reflected background method (Berge et al. 2007) is used to define the OFF regions. The excess of γ-rays in the ON region is statistically highly significant (Li & Ma 1983): 21.5σ for the pre-flare period and 22.0σ for the flare. Statistics are summarized in Table 1.

The differential energy spectrum of the VHE γ-ray emission has been derived using a forward-folding method (Piron et al. 2001). For the observations prior to 2012 April, a power

[45] PG 1553+113 has one of the steepest spectra measured at VHE.
[46] The difference of energy threshold between the two data set is due to the changing observation conditions, e.g., zenith angle and optical efficiency.

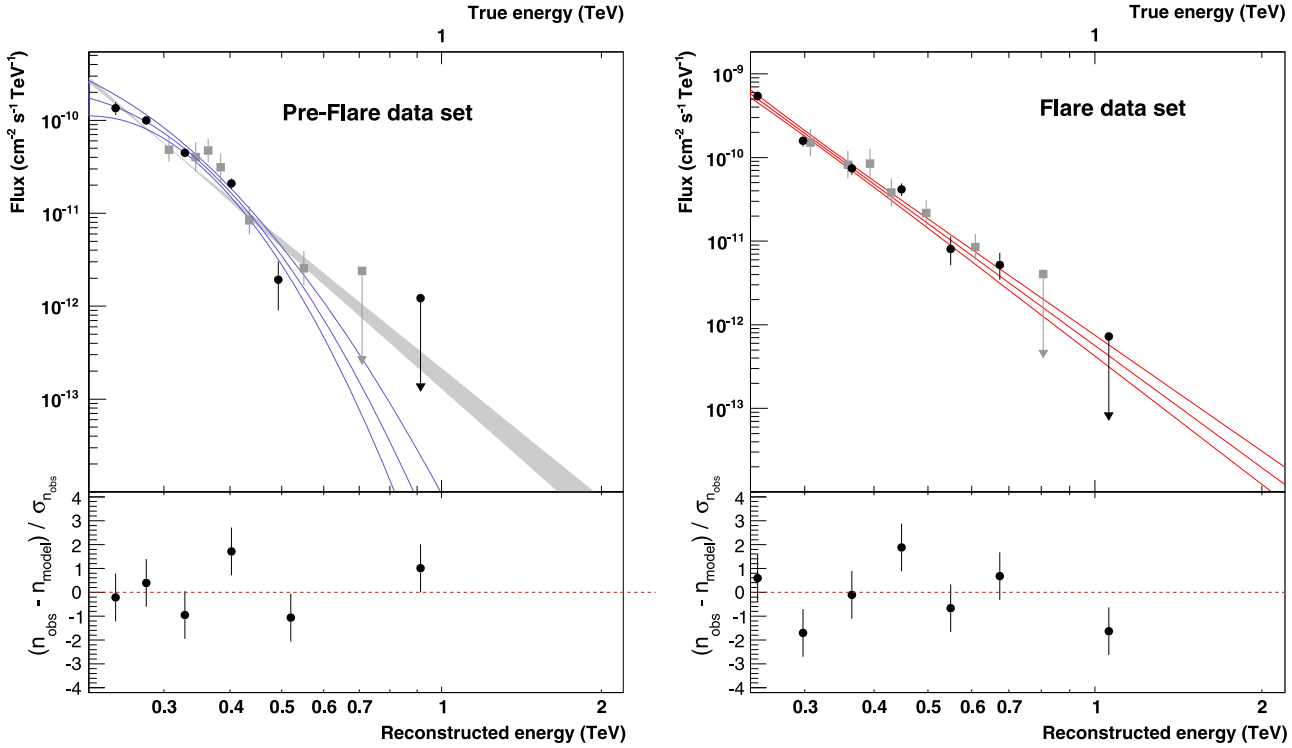

Figure 1. Differential fluxes of PG 1553+113 during the pre-flare (left) and flare (right) periods. Error contours indicate the 68% uncertainty on the spectrum. Uncertainties on the spectral points (in black) are given at 1σ level, and upper limits are computed at the 99% confidence level. The gray squares were obtained by the cross-check analysis chain and are presented to visualize the match between both analyses. The gray error contour on the left panel is the best-fit power law model. The lower panels show the residuals of the fit, i.e., the difference between the measured (n_{obs}) and expected numbers of photons (n_{model}), divided by the statistical error on the measured number of photons ($\sigma_{n_{obs}}$).

law (PWL) model fitted to the data gives a χ^2 of 51.7 for 40 degrees of freedom (dof, corresponding to a χ^2 probability of $P_{\chi^2} = 0.10$). The values of the spectral parameters (see Table 2) are compatible with previous analyses by H.E.S.S. covering the same period (Aharonian et al. 2008). A log-parabola (LP) model,[47] with a χ^2 of 37.5 for 39 dof ($P_{\chi^2} = 0.54$), is found to be preferred over the PWL model at a level of 4.3σ using the log-likelihood ratio test. Note that systematic uncertainties, presented in Table 2, have been evaluated by Aharonian et al. (2006b) for the PWL model and using the jack-knife method for the LP model. The jack-knife method consists in removing one run and redoing the analysis. This process is repeated for all runs.

For the flare data set, the LP model does not significantly improve the fit and the simple PWL model describes the data well, with a χ^2 of 33.0 for 23 dof ($P_{\chi^2} = 0.08$). Table 2 contains the integral fluxes above the reference energy of 300 GeV. The flux increased by a factor of ~3 in the flare data set compared to the pre-flare one with no sign of spectral variations (when comparing power law fits for both data sets). The derived spectra and error contours for each data set are presented in Figure 1, where the spectral points obtained from the cross-check analysis are also plotted.

To compute the light curves, the integrated flux above 300 GeV for each observation run was extracted using the corresponding (pre-flare or flare) best fit spectral model. A fit with a constant of the run-wise light curve of the entire (pre-flare+flare) data set, weighted by the statistical errors, yields a χ^2 of 123.2 with 68 dof ($P_{\chi^2} = 6.6 \times 10^{-5}$). Restricting the analysis to the pre-flare data set only, the fit yields a χ^2 of 51.76 with 60 dof ($P_{\chi^2} = 0.77$), indicating again a flux increase detected by H.E.S.S. at the time of the flaring activity reported by Cortina (2012b).

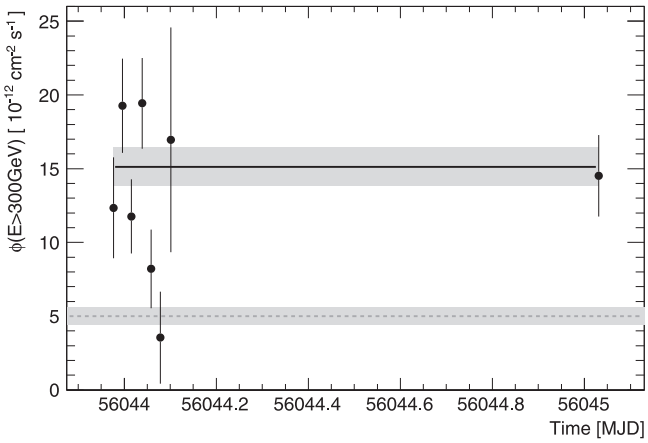

Figure 2. H.E.S.S. light curve of PG 1553+113 during the two nights of the flare period. The continuous line is the measured flux during the flare period while the dashed one corresponds to the pre-flare period (see Table 2 for the flux values). Gray areas are the 1σ errors.

Figure 2 shows the light curve during the flare together with the averaged integral fluxes above 300 GeV of both data sets. A fit with a constant to the H.E.S.S. light curve during the first night yields a χ^2 of 20.76 for 6 dof ($P_{\chi^2} = 2.0 \times 10^{-3}$), indicating intra-night variability. This is also supported by the

[47] The log-parabola is defined by $dN/dE = \Phi_0 (E/E_0)^{-a-b\log(E/E_0)}$.

Table 3
Results of the *Fermi*-LAT Data Analysis for the Pre-flare and Flare Periods

MJD Range	Energy Range (GeV)	TS	Spectral Parameters	$I(E > 300\text{MeV})$ (10^{-8} (ph cm^{-2} s^{-1})
54682–55987	0.3–300	7793.7	$a = 1.49 \pm 0.06_{\text{stat}} \pm 0.01_{\text{sys}}$ $b = 3.8 \pm 1.1_{\text{stat}} \pm 0.1_{\text{sys}}$	$2.82 \pm 0.1_{\text{stat}} \pm 0.2_{\text{sys}}$
56040–56047	0.3–300	43.8	$\Gamma = 1.78 \pm 0.24_{\text{stat}} \pm 0.01_{\text{sys}}$	$3.5 \pm 1.3_{\text{stat}} \pm 0.3_{\text{sys}}$
56040–56047	0.3–80	44.5	$\Gamma = 1.72 \pm 0.26_{\text{stat}} \pm 0.01_{\text{sys}}$	$3.4 \pm 1.3_{\text{stat}} \pm 0.3_{\text{sys}}$

Note. For the flare period, the analysis has been performed in two energy ranges (see Section 3.2). The first two columns give the time and energy windows and the third the corresponding Test Statistic (TS) value. The model parameters and the flux above 300 MeV are given in the last two columns. The systematic uncertainties were computed using the IRFs bracketing method (Abdo et al. 2009a).

use of a Bayesian block algorithm (Scargle 1998) that finds three blocks for the two nights at a 95% confidence level.

2.2. *Fermi*-LAT Analysis

The *Fermi*-LAT is detector converting γ-rays to e^+e^- pairs (Atwood et al. 2009). The LAT is sensitive to γ-rays from 20 MeV to >300 GeV. In survey mode, in which the bulk of the observations are performed, each source is seen every 3 hr for approximately 30 minutes.

The *Fermi*-LAT data and software are available from the *Fermi* Science Support Center.[48] In this work, the ScienceTools `V9R32P5` were used with the Pass 7 reprocessed data (Bregeon et al. 2013), specifically `SOURCE` class event (Ackermann et al. 2012a), with the associated `P7REP_SOURCE_V15` instrument response functions. Events with energies from 300 MeV to 300 GeV were selected. Additional cuts on the zenith angle (<100°) and rocking angle (<52°) were applied as recommended by the LAT collaboration[49] to reduce the contamination from the Earth atmospheric secondary radiation.

The analysis of the LAT data was performed using the `Enrico` Python package (Sanchez & Deil 2013). The sky model was defined as a region of interest of 15° radius with PG 1553+113 in the center and additional point-like sources from the internal 4 yr source list. Only the sources within a 3° radius around PG 1553+113 and bright sources (integral flux greater than 5×10^{-7} ph cm^{-2} s^{-1}) had their parameters free to vary during the likelihood minimization. The template files `isotrop_4years_P7_V15_repro_v2_source.txt` for the isotropic diffuse component, and `template_4years_P7_v15_repro_v2.fits` for the standard Galactic model, were included. A binned likelihood analysis (Mattox et al. 1996), implemented in the `gtlike` tool, was used to find the best-fit parameters.

As for the H.E.S.S. data analysis, two spectral models were used: a simple PWL and a LP. A likelihood ratio test was used to decide which model best describes the data. Table 3 gives the results for the two time periods considered in this work, and Figure 3 presents the γ-ray spectral energy distributions. The first one (pre-flare), before the H.E.S.S. exposures in 2012, includes more than 3.5 yr of data (from 2008 August 4 to 2012 March 1). The best fit model is found to be the LP (with a Test Statistic[50] of 11.3, $\approx 3.4\sigma$). The second period (flare) is centered on the H.E.S.S. observation windows and lasts for 7 days. The best fit model is a power law, the flux being consistent with the one measured during the first 3.5 yr. Data points or light curves were computed within a restricted energy range or time range using a PWL model with the spectral index frozen to 1.70.

To precisely probe the variability in HE γ-rays, 7-day time bins were used to compute the light curve of PG 1553+113 in an extended time window (from 2008 August 4 to 2012 October 30), to probe any possible delay of a HE flare with respect to the VHE one. While the flux of PG 1553+113 above 300 MeV is found to be variable in the whole period with a variability index of $F_{\text{var}} = 0.16 \pm 0.04$ (Vaughan et al. 2003), there is no sign of any flaring activity around the 2012 H.E.S.S. observations. This result has been confirmed by using the Bayesian block algorithm, which finds no block around the H.E.S.S. exposures in 2012. Similar results were obtained when considering only photons with an energy greater than 1 GeV. No sign of enhancement of the HE flux associated to the VHE event reported here was found. This might be due to the lack of statistics at high energy in the LAT energy range.

3. DISCUSSION OF THE RESULTS

3.1. Variability in γ-rays

The VHE data do not show any sign of variation of the spectral index (when comparing flare and pre-flare data sets with the same spectral model), and in HE no counterpart of this event can be found. The indication for intra-night variability is similar to other TeV HBLs (Mrk 421, Mrk 501 or PKS 2155-304) with, in this case, flux variations of a factor 3.

As noticed in previous works, PG 1553+113 presents a sharp break between the HE and VHE ranges (Abdo et al. 2010a) and the peak position of the γ-ray spectrum in the $\nu f(\nu)$ representation is located around 100 GeV. This is confirmed by the fact that the LP model better represents the pre-flare period in HE. Nonetheless, the precise location of this peak cannot be determined with the *Fermi*-LAT data only. Combining both energy ranges and fitting the HE and VHE data points with a power law with an exponential cutoff[51] allows us to determine the $\nu f(\nu)$ peak position for both time periods. The functional form of the model is

$$E^2 \frac{dN}{dE} = N \left(\frac{E}{100\ \text{GeV}} \right)^{-\Gamma} \exp\left(-E/E_c\right).$$

[48] http://fermi.gsfc.nasa.gov/ssc/data/analysis/

[49] http://fermi.gsfc.nasa.gov/ssc/data/analysis/documentation/Cicerone/index.html

[50] Here the TS is two times the difference between the log-likelihood of the fit with a LP minus the log-likelihood with a PL.

[51] A fit with a LP model has been attempted, but the power law with an exponential cutoff leads to a better description of the data.

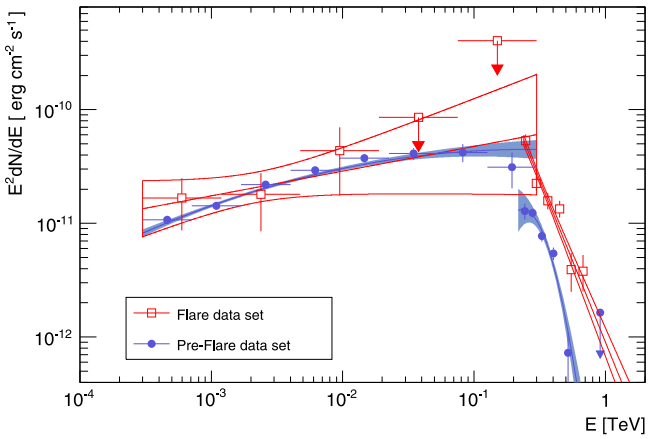

Figure 3. Spectral energy distribution of PG 1553+113 in γ-rays as measured by the *Fermi*-LAT and H.E.S.S. Red (blue) points and butterflies have been obtained during the flare (pre-flare) period. The *Fermi* and H.E.S.S. data for the pre-flare are not contemporaneous. H.E.S.S. data were taken in 2005–2006 while the *Fermi* data were taken between 2008 and 2012.

For this purpose, *Fermi*-LAT and H.E.S.S. systematic uncertainties were taken into account in a similar way as in Abramowski et al. (2014) and added quadratically to the statistical errors. The *Fermi*-LAT systematic uncertainties were estimated by Ackermann et al. (2012a) to be 10% of the effective area at 100 MeV, 5% at 316 MeV and 15% at 1 TeV and above. For the VHE γ-ray range, they were taken into account by shifting the energy by 10%. This effect translates into a systematic uncertainty for a single point of $\sigma(f)_{\rm sys} = 0.1 \cdot \partial f / \partial E$ where f is the differential flux at energy E.

The results of this parameterization are given in Table 4. Using the pre-flare period, the peak position is found to be located at $\log_{10}(E_{\rm max}/1\ {\rm GeV}) = 1.7 \pm 0.2_{\rm stat} \pm 0.4_{\rm sys}$ with no evidence of variation during the flare and no spectral variation. This is consistent with the fact that no variability in HE γ-rays was found during the H.E.S.S. observations. This is also in agreement with the fact that HBLs are less variable in HE γ-rays than other BL Lac objects (Abdo et al. 2010b), while numerous flares have been reported in the TeV band.

3.2. Constraints on the Redshift

The EBL is a field of UV to far-infrared photons produced by the thermal emission from stars and reprocessed starlight by dust in galaxies (see Hauser & Dwek 2001, for a review) that interacts with very high energy γ-rays from sources at cosmological distances. As a consequence, a source at redshift z exhibits an observed spectrum $\phi_{\rm obs}(E) = \phi_{\rm int}(E) \times e^{-\tau(E,z)}$ where $\phi_{\rm int}(E)$ is the intrinsic source spectrum and τ is the optical depth due to interaction with the EBL. Since the optical depth increases with increasing γ-ray energy, the integral flux is lowered and the spectral index is increased.[52] In the following, the model of Franceschini et al. (2008) was used to compute the optical depth τ as a function of redshift and energy. In this section, the data taken by both instruments during the flare period are used, with the *Fermi*-LAT analysis restricted to the range 300 MeV < E < 80 GeV (see Table 3 for the results). In the modest redshift range of VHE emitters detected so far ($z \leqslant 0.6$), the EBL absorption is negligible below 80 GeV ($\tau_{\gamma\gamma} \sim 0.1$ at 80 GeV for $z = 0.6$).

A measure of the EBL energy density was obtained by Ackermann et al. (2012b) and Abramowski et al. (2013b) based on the spectra of sources with a known z. In the case of PG 1553+113, for which the redshift is unknown, the effects of the EBL on the VHE spectrum might be used to derive constraints on its distance. Ideally, this would be done by comparing the observed spectrum with the intrinsic one but the latter is unknown. The *Fermi*-LAT spectrum, derived below 80 GeV, can be considered as a proxy for the intrinsic spectrum in the VHE regime, or at least, as a solid UL (assuming no hardening of the spectrum).

Following the method used by Abramowski et al. (2013a), it has been assumed that the intrinsic spectrum of the source in the H.E.S.S. energy range cannot be harder than the extrapolation of the *Fermi*-LAT measurement. From this, one can conclude that the optical depth cannot be greater than $\tau_{\rm max}(E)$, given by:

$$\tau_{\rm max}(E) = \ln\left[\frac{\phi_{\rm int}}{(1-\alpha)\left(\phi_{\rm obs} - 1.64\Delta\phi_{\rm obs}\right)}\right], \quad (1)$$

where $\phi_{\rm int}$ is the extrapolation of the *Fermi*-LAT measurement toward the H.E.S.S. energy range. $\phi_{\rm obs} \pm \Delta\phi_{\rm obs}$ is the flux measured by H.E.S.S. The factor $(1-\alpha) = 0.8$ accounts for the systematic uncertainties of the H.E.S.S. measurement and the number 1.64 has been calculated to have a confidence level of 95% (Abramowski et al. 2013a). The comparison is made at the H.E.S.S. decorrelation energy where the flux is best measured.

Figure 4 shows the 95% UL on $\tau_{\rm max}$. The resulting UL on the redshift is $z < 0.43$. This method does not allow the statistical and systematic uncertainties of the *Fermi*-LAT measurement to be taken into account and does not take advantage of the spectral features of the absorbed spectrum (see Abramowski et al. 2013b).

A Bayesian approach has been developed with the aim of taking all the uncertainties into account. It also uses the fact that EBL-absorbed spectra are not strictly power laws. The details of the model are presented in Appendix A and only the main assumptions and results are recalled here. Intrinsic curvature between the HE and VHE ranges that naturally arises due to either curvature of the emitting distribution of particles or emission effects (e.g., Klein–Nishina effects) is permitted by construction of the prior (Equation (A.1)). A spectral index softer than the *Fermi*-LAT measurement is allowed with a constant probability, in contrast with the previous calculation. It is assumed that the observed spectrum in VHE γ-rays cannot be harder than the *Fermi*-LAT measurement by using a prior that follows a Gaussian for indices harder than the *Fermi*-LAT one. The prior on the index is then:

$$P(\Gamma) \propto \mathcal{N}_G\left(\Gamma, \Gamma_{\rm Fermi}, \sigma_\Gamma\right) \quad (2)$$

if $\Gamma < \Gamma_{\rm Fermi}$ and

$$P(\Gamma) \propto 1$$

otherwise. $\Gamma_{\rm Fermi}$ is the index measured by *Fermi*-LAT and σ_Γ is the uncertainty on this measurement that takes all the systematic and statistical uncertainties into account.

[52] For sake of simplicity it is assumed here that the best-fit model is a power law, an assumption which is true for most of the cases due to limited statistics in the VHE range.

Table 4
Parametrization Results of the Two Time Periods (First Column) Obtained by Combining H.E.S.S. and *Fermi*-LAT

Period	N ($E = 100$ GeV) (10^{-11} erg cm^{-2} s^{-1})	Γ	$\log_{10}(E_c/1\ \mathrm{GeV})$	$\log_{10}(E_{max}/1\ \mathrm{GeV})$
Pre-flare	$9.6 \pm 0.7_{stat} \pm 1.7_{sys}$	$1.59 \pm 0.02_{stat} \pm 0.03_{sys}$	$2.03 \pm 0.02_{stat} \pm 0.04_{sys}$	$1.7 \pm 0.2_{stat} \pm 0.4_{sys}$
Flare	$13.0 \pm 3.5_{stat} \pm 5.7_{sys}$	$1.56 \pm 0.08_{stat} \pm 0.11_{sys}$	$2.16 \pm 0.04_{stat} \pm 0.09_{sys}$	$1.8 \pm 0.7_{stat} \pm 1.3_{sys}$

Note. The second column gives the normalization at 100 GeV, while the third and the fourth present the spectral index and cut-off energy of the fitted power law with an exponential cut-off. The last column is the peak energy in a $\nu f(\nu)$ representation.

Table 5
Calibrated 95% 1-Sided LL and UL (including systematic errors) on the Dispersion Parameter τ_n and Derived 95% one-sided Lower Limits on E_{QG}

	Limits on τ_n (s TeV^{-n})		Lower Limits on E_{QG} (GeV)	
n	LL$^{calib+syst}$	UL$^{calib\ +\ syst}$	$s = -1$	$s = +1$
1	−838.9	576.4	2.83×10^{17}	4.11×10^{17}
2	−1570.5	1012.4	1.68×10^{10}	2.10×10^{10}

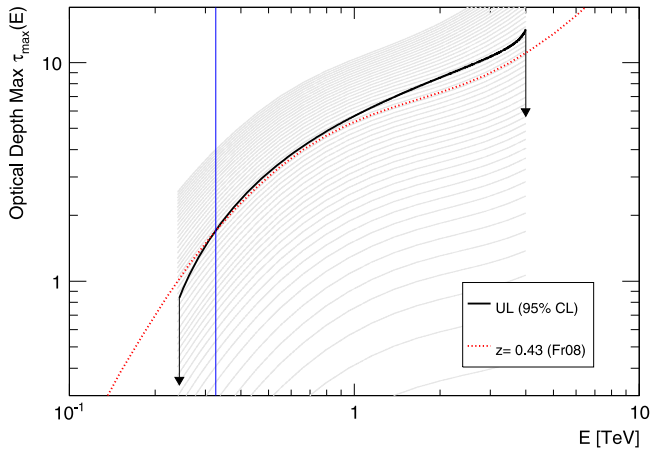

Figure 4. Values of τ_{max} as a function of the photon energy. The black line is the 95% UL obtained with the H.E.S.S. data and the red line is the optical depth computed with the model of Franceschini et al. (2008) for a redshift of 0.43. The blue line is the decorrelation energy for the H.E.S.S. analysis. The gray lines are the value of optical depth for different redshifts.

The most probable redshift found with this method is $z = 0.49 \pm 0.04$, in good agreement with the independent measure of Danforth et al. (2010), who constrained the distance to be between $0.43 < z < 0.58$. Figure 5 gives the posterior probability obtained with the Bayesian method compared with other measurements of z. Lower and upper limits at a confidence level of 95% can also be derived as $0.41 < z < 0.56$. Note that this method allows the systematic uncertainties of both instruments (*Fermi*-LAT and H.E.S.S.) to be taken into account. The spectral index obtained when fitting the H.E.S.S. data with an EBL absorbed PWL using a redshift of 0.49 is compatible with the *Fermi* measurement below 80 GeV.

3.3. Lorentz Invariance Violation

As stated in Section 2.1, the H.E.S.S. data of the flare show an indication of intra-night variability, which is used here to test for a possible LIV. Some Quantum Gravity (QG) models predict a change of the speed of light at energies close to the Planck scale ($\sim 10^{19}$ GeV). A review of such models can be found in Mattingly (2005) and Liberati (2013). An energy-dependent dispersion in vacuum is searched for in the data by testing a correlation between arrival times of the photons and their energies. For two photons with arrival times t_1 and t_2 and energies E_1 and E_2, the dispersion parameter of order n is defined as $\tau_n = \frac{t_2 - t_1}{E_2^n - E_1^n} = \frac{\Delta t}{\Delta(E^n)}$. Here only the linear ($n = 1$) and quadratic ($n = 2$) dispersion parameters are calculated. Assuming no intrinsic spectral variability of the source, the dispersion τ_n can be related to the normalized distance of the source κ_n corrected for the expansion of the universe and an energy E_{QG} at which QG effects are expected to occur (Jacob & Piran 2008):

$$\tau_n = \frac{\Delta t}{\Delta(E^n)} \simeq s_{\pm}\frac{(1+n)}{E_{QG}^n 2H_0}\kappa_n \quad (3)$$

where H_0 is the Hubble constant and $s_{\pm} = -1$ (resp. +1) in the superluminal (resp. subluminal) case, in which the high-energy photons arrive before (resp. after) low-energy photons. The normalized distance κ_n is calculated from the redshift of the source z and the cosmological parameters Ω_m, Ω^{Λ} given in the introduction:

$$\kappa_n = \int_0^z \frac{(1+z')^n\, dz'}{\sqrt{\Omega_m(1+z')^3 + \Omega_{\Lambda}}} \quad (4)$$

Using the central value of $z = 0.49$ determined in Section 3.2, the distance κ_n for $n = 1$ and 2 is $\kappa_1 = 0.541$ and $\kappa_2 = 0.677$.

First, the dispersion measurement method will be described. It will then be applied to the H.E.S.S. flare dataset (Monte Carlo (MC) simulations and original dataset), in order to measure the dispersion and provide 95% 1-sided lower and upper limits on the dispersion parameter τ_n. These limits on τ_n will lead to lower limits (LLs) on E_{QG} using Equation (3).

3.3.1. Modified Maximum Likelihood Method

A maximum likelihood method, following Martinez & Errando (2009), was used to calculate the dispersion parameter τ_n. Albert et al. (2008) applied this method to a flare of Mkn 501, while Abramowski et al. (2011) applied it to a flare of PKS 2155-304. More recently, it was used by Vasileiou et al. (2013) to analyze *Fermi* data of four gamma-ray bursts. The data from Cherenkov telescopes are contaminated by π^0 decay from proton showers, misidentified electrons, or heavy elements such as helium. In the case of PG 1553+113, and contrary to previous analyses, this background is not negligible: the signal-over-background ratio S/B is about 2, compared to 300 for the PKS 2155-304 flare event of 2006 July (Aharonian et al. 2007b). The background was included in the formulation of the probability density function (PDF) used in a likelihood maximization method. Given the times t_i and energies E_i of the gamma-like (ON) particles received by the

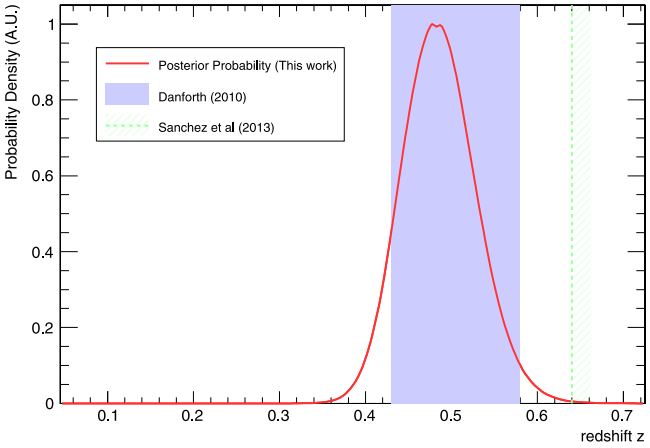

Figure 5. Posterior probability density as a function of redshift (red). The blue area represents the redshift range estimated by Danforth et al. (2010) while the green dashed line indicates the limit of Sanchez et al. (2013).

detector, the unbinned likelihood function of the dispersion parameter τ_n is:

$$L(\tau_n) = \prod_{i=1}^{n_{\rm ON}} P\left(E_i, t_i \middle| \tau_n\right). \quad (5)$$

The PDF $P(E_i, t_i|\tau_n)$ associated with each ON event is composed of two terms:

$$P\left(E_i, t_i \middle| \tau_n\right) = w_s \cdot P_{\rm Sig}\left(E_i, t_i \middle| \tau_n\right) + \left(1 - w_s\right) \cdot P_{\rm Bkg}\left(E_i, t_i\right) \quad (6)$$

with

$$P_{\rm Sig}\left(E_i, t_i \middle| \tau_n\right) = \frac{1}{N(\tau_n)} A_{\rm eff}\left(E_i, t_i\right) \times \Lambda_{\rm Sig}\left(E_i\right) F_{\rm Sig}\left(t_i - \tau_n \cdot E_i^n\right) \quad (7)$$

$$P_{\rm Bkg}\left(E_i, t_i\right) = \frac{1}{N'} A_{\rm eff}\left(E_i, t_i\right) \Lambda_{\rm Bkg}\left(E_i\right) F_{\rm Bkg} \quad (8)$$

$$w_s = \frac{n_{\rm ON} - \alpha\, n_{\rm OFF}}{n_{\rm ON}}. \quad (9)$$

The PDF $P_{\rm Sig}$ includes the emission time distribution of the photons $F_{\rm Sig}$ determined from a parameterization of the observed light curve at low energies (discussed in the next section) and evaluated on $t - \tau_n \cdot E^n$ to take into account the delay due to a possible LIV effect, the measured signal spectrum $\Lambda_{\rm Sig}$ and the effective area $A_{\rm eff}$. The PDF $P_{\rm Bkg}$ is composed of the uniform time distribution $F_{\rm Bkg}$ of the background events, the measured background spectrum $\Lambda_{\rm Bkg}$ and the effective area $A_{\rm eff}$. No delay due to a possible LIV effect is expected in the background events of the ON data set. $N(\tau_n)$ and N' are the normalization factors of $P_{\rm Sig}$ and $P_{\rm Bkg}$ respectively, in the (E, t) range of the likelihood fit. The coefficient w_s corresponds to the relative weight of the signal events in the total ON data set, derived from the number of events in the ON region $n_{\rm ON}$ and the number of events in the OFF regions $n_{\rm OFF}$ weighted by the inverse number of OFF regions α. More details on the derivation of this function are given in Appendix B.1.

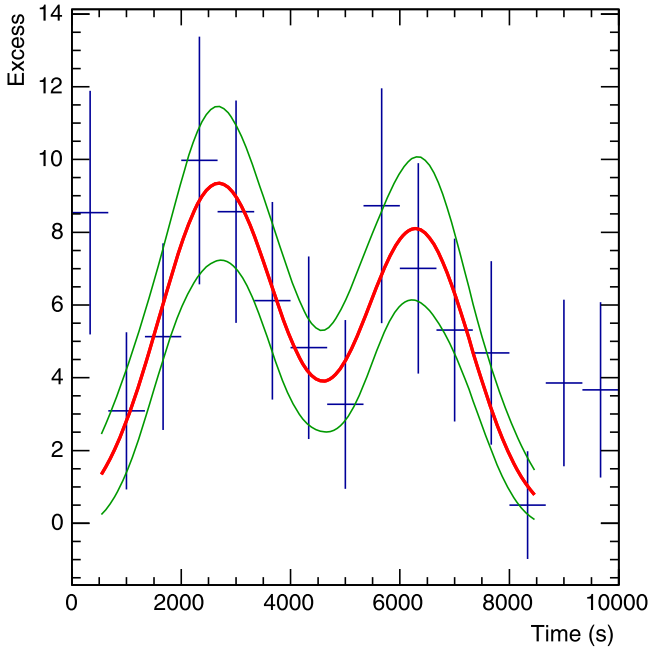

Figure 6. Time distribution of the excess ON − αOFF in the first six runs (70971–70976), with energies between 300 and 400 GeV. $T = 0$ corresponds to the time of the first detected event in run 70971. The vertical bars correspond to 1σ statistical errors; the horizontal bars correspond to the bin width in time. The best fit, in red, was used as the template light curve in the maximum likelihood method; the $\pm 1\sigma$ error envelope is shown in green.

3.3.2. Specific Selection Cuts and Timing Model

The flare data set of the H.E.S.S. analysis (see Section 2.1) was used with additional cuts. To perform the dispersion studies, only uninterrupted data have been kept. Thus, the analysis was conducted on the first seven runs, taken during the night of April 26. Moreover, the cosmic ray flux increases substantially for the seventh run, due to a variation of the zenith angle during this night. This fact, along with its large statistical errors, leads us to discard this run from the analysis. The sixth run shows little to no variability and was therefore also removed from the LIV analysis. Since within the ON data set, the signal and the background spectra have different indices ($\Gamma_{\rm Sig} = 4.8$ for the signal and $\Gamma_{\rm Bkg} = 2.5$ for the background), the ratio S/B is expected to decrease with increasing energy. An upper energy cut at $E_{\rm max} = 789$ GeV was set, corresponding to the last bin with more than 3σ significance in the reconstructed photon spectrum (see the differential flux during the flare in Figure 1). A lower cut on the energy at $E_{\rm min} = 300$ GeV was used in order to avoid large systematic effects arising from high uncertainties on the H.E.S.S. effective area at lower energies. The intrinsic light curve of the flare, needed in the formulation of the likelihood, can be obtained from a model of the timed emission or approximated from a subset of the data. To be as model-independent as possible, it was here derived from a fit of the measured light curve at low energies (with $E < E_{\rm cut}$). The high-energy events ($E > E_{\rm cut}$) were processed in the calculation of the likelihood to search for potential dispersion. Here $E_{\rm cut}$ was set to $E_{\rm cut} = 400$ GeV, which is approximately the median energy of the ON event sample. Other cuts on the energy did not introduce significant effects on the final results. The histogram and the fit (Figure 6) were obtained as follows: the main idea was to preserve the maximum detected variability

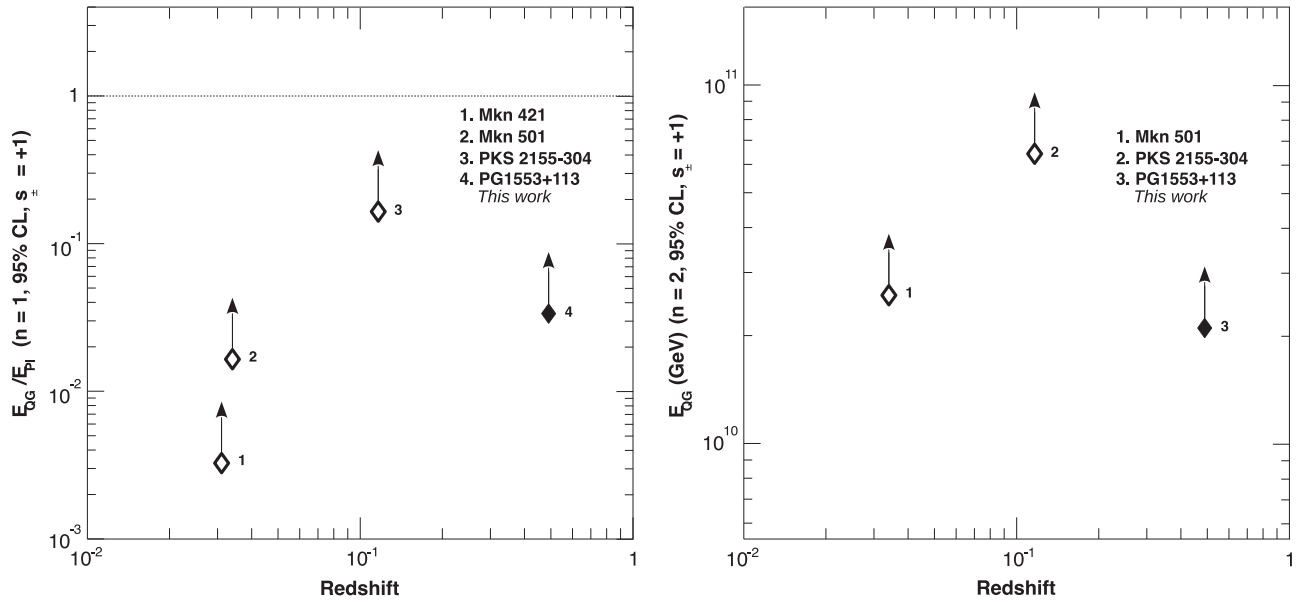

Figure 7. Lower limits on $E_{QG,1}$ from linear dispersion (left) and on $E_{QG,2}$ from quadratic dispersion (right) for the subluminal case ($s = +1$) obtained with AGNs as a function of redshift. The limits are given in terms of E_{Planck}. The constraints from Mkn 421 have been obtained by Biller et al. (1999), from Mkn 501 by Albert et al. (2008), and from PKS 2155-304 by Abramowski et al. (2011).

in the PG 1553+113 flare, together with a significant response in each observed peak:

1. The binning was chosen so that at least two adjacent bins of the distribution yield a minimum of 3σ excess with respect to the average value.
2. Simple parameterizations have been tested on the whole data set (all energies): constant (χ^2/dof = 25/12), single Gaussian (χ^2/dof = 20/10) and double Gaussian (χ^2/dof = 8.5/7) functions. The latter is preferred, since it improves the quality of the fit. This shape was chosen to fit the low energy subset of events. Choosing a single Gaussian parameterization would result in a decrease of the sensitivity to time-lag measurements by a factor of two.

There is a gap of ~2 minutes between each two consecutive runs. We did not consider the effect of these gaps as it is small with respect to the bin width of ~10 minutes. More importantly, their occurrence is not correlated with the binning: one gap falls in the rising part of the light curve, one is at a maximum, two fall in the decreasing parts and none of the gaps is at the minimum.

Table B1 in Appendix B.2 shows the number of ON and OFF events for the different cuts applied to the data.

3.3.3. Results: Limits on τ_n and E_{QG}

The maximum likelihood method was performed using high-energy events with $E_i > E_{cut}$. First, confidence intervals (CIs) corresponding to 95% confidence level (1-sided) were determined from the likelihood curve at the values of τ_n where the curve reaches 2.71, which corresponds to the 90% CL quantile of a χ^2 distribution. However, these CIs are derived from one realization only and do not take into account the "luckiness" factor of this measurement. To get statistically significant CIs ("calibrated CIs"), several sets were generated with MC simulations, with the same statistical significance, light curve model and spectrum as the original data set. No intrinsic dispersion was artificially added. Each simulated data set produces a LL and an UL on τ_n. The calibrated lower (upper) limit of the confidence interval is obtained from the mean of the distribution of the per-set individual lower (upper) limits. Both CIs (from the data only and from the simulated sets) are listed in Table B2. Sources of systematic errors include uncertainties on the light curve parameterization, the background contribution, the calculation of the effective area, the energy resolution, and the determination of the photon index (see Appendix B.4).

The resulting limits on the dispersion τ_n using the quadratic sum of the statistical errors from the simulations and the systematic errors determined from data and simulations were computed, leading to limits on the energy scale E_{QG} (Equation (3)). The 95% 1-sided LLs for the subluminal case ($s = +1$) are: $E_{QG,1} > 4.11 \times 10^{17}$ GeV and $E_{QG,2} > 2.10 \times 10^{10}$ GeV for linear and quadratic LIV effects, respectively. For the superluminal case ($s = -1$) the limits are: $E_{QG,1} > 2.83 \times 10^{17}$ GeV and $E_{QG,2} > 1.68 \times 10^{10}$ GeV for linear and quadratic LIV effects, respectively. Figure 7 shows a comparison of the different LLs on $E_{QG,1}$ and $E_{QG,2}$ for the subluminal case ($s = +1$) obtained with AGNs at different redshifts studied at VHE. All these limits, including the present results, have been obtained under the assumption that no intrinsic delays between photons of different energies occur at the source. For the linear/subluminal case, the most constraining limit on E_{QG} with transient astrophysical events has been obtained with GRB 090510: $E_{QG,1} > 6.3 \times 10^{19}$ GeV (Vasileiou et al. 2013). The most constraining limits on E_{QG} with AGN so far have been obtained by Abramowski et al. (2011) with PKS 2155-304 data observed with H.E.S.S.: $E_{QG,1} > 2.1 \times 10^{18}$ GeV and $E_{QG,2} > 6.4 \times 10^{10}$ GeV for linear and quadratic LIV effects, respectively (95% CL, 1-sided). Compared to the PKS 2155-304 limits, the limits on the linear dispersion for PG 1553+113 are one order of magnitude less constraining, but the limits on the quadratic dispersion are of the same order of magnitude since the source is located at a higher redshift. This highlights the interest in studying distant AGNs, in spite of the difficulties due to limited photon statistics.

4. CONCLUSIONS

A VHE γ-ray flaring event of PG 1553+113 has been detected with the H.E.S.S. telescopes, with a flux increasing by a factor of 3. No variability of the spectral index has been found in the data set, but indication of intra-night flux variability is reported in this work. In HE γ-rays, no counterpart of this event can be identified, which may be interpreted as the sign of injection of high energy particles emitting predominantly in VHE γ-rays. Such particles might not be numerous enough to have a significant impact on the HE flux during either their acceleration or cooling phases.

The data were used to constrain the redshift of the source using a new approach based on the absorption properties of the EBL imprinted in the spectrum of a distant source. Taking into account all the instrumental systematic uncertainties, the redshift of PG 1553+113 is determined as being $z = 0.49 \pm 0.04$.

Flares of variable sources can be used to probe LIV effects, manifesting themselves as an energy-dependent delay in the photon arrival time. A likelihood method, adapted to flares with a large amount of background and modest statistics, was presented. To demonstrate the analysis power of this method, it was applied to the H.E.S.S. data of a flare of PG 1553+113. This analysis relies on the indication of the intra-night variability of the flare at VHE. No significant dispersion was measured, and limits on the $E_{\rm QG}$ scale were derived, in a region of redshift unexplored until now. Limits on the energy scale at which QG effects causing LIV may arise, derived in this work, are $E_{\rm QG,1} > 4.11 \times 10^{17}$ GeV and $E_{\rm QG,2} > 2.10 \times 10^{10}$ GeV for the subluminal case. Compared with previous limits obtained with the PKS 2155-304 flare of 2006 July, the limits for PG 1553+113 for a linear dispersion are one order of magnitude less constraining while limits for a quadratic dispersion are of the same order of magnitude. With the new telescope placed at the center of the H.E.S.S. array that provides an energy threshold of several tens of GeV, a better picture of the variability patterns of AGN flares should be obtained. The future Cherenkov Telescope Array will increase the number of flare detections (Sol et al. 2013) with better sensitivity, allowing for the extraction of even more constraining limits on the LIV effects.

The support of the Namibian authorities and of the University of Namibia in facilitating the construction and operation of H.E.S.S. is gratefully acknowledged, as is the support by the German Ministry for Education and Research (BMBF), the Max Planck Society, the French Ministry for Research, the CNRS-IN2P3 and the Astroparticle Interdisciplinary Programme of the CNRS, the UK Particle Physics and Astronomy Research Council (PPARC), the IPNP of the Charles University, the South African Department of Science and Technology and National Research Foundation, and the University of Namibia. We appreciate the excellent work of the technical support staff in Berlin, Durham, Hamburg, Heidelberg, Palaiseau, Paris, Saclay, and Namibia in the construction and operation of the equipment.

The *Fermi* LAT Collaboration acknowledges generous ongoing support from a number of agencies and institutes that have supported both the development and the operation of the LAT as well as scientific data analysis. These include the National Aeronautics and Space Administration and the Department of Energy in the United States, the Commissariat à l'Energie Atomique and the Centre National de la Recherche Scientifique/Institut National de Physique Nucléire et de Physique des Particules in France, the Agenzia Spaziale Italiana and the Istituto Nazionale di Fisica Nucleare in Italy, the Ministry of Education, Culture, Sports, Science and Technology (MEXT), High Energy Accelerator Research Organization (KEK) and Japan Aerospace Exploration Agency (JAXA) in Japan, and the KA Wallenberg Foundation, the Swedish Research Council and the Swedish National Space Board in Sweden. Additional support for science analysis during the operations phase is gratefully acknowledged from the Istituto Nazionale di Astrofisica in Italy and the Centre National d'Etudes Spatiales in France. DS work is supported by the LABEX grant enigmass. The authors want to thank F. Krauss for her useful comments.

APPENDIX A
BAYESIAN MODEL USED TO CONSTRAIN THE REDSHIFT

A Bayesian approach has been used to compute the redshift value of PG 1553+113 in Section 3.2. The advantage of such a model is that systematic uncertainties, which are important in Cherenkov astronomy, can easily be included in the calculation. In the following, the notation Θ for the model parameters and Y for the data set is adopted. All normalization constants are dropped in the development of the model, and the final probability is normalized at the end.

Bayes' Theorem, based on the conditional probability rule, allows us to write the posterior probability $P(\Theta|Y)$ for the model parameters Θ as the product of the likelihood $P(Y|\Theta)$ and the prior probability $P(\Theta)$:

$$P(\Theta|Y) \propto P(\Theta)P(Y|\Theta).$$

The likelihood is the quantity that is maximized during determination of the best-fit spectrum (Piron et al. 2001). It is at this step that the H.E.S.S. data, taken during the flare, were actually used. The spectrum model here is a simple power law corrected for the EBL absorption:

$$\phi = N \times \left(E/E_0\right)^{-\Gamma} \times e^{-\tau(E,z)}.$$

The model parameters are then N, Γ, and z.

The prior is the most difficult and most interesting part of the model. To derive it, N and Γ are assumed to be independent from each other and independent of the redshift. In contrast, the prior on the redshift might depend on N and Γ. Then, the prior can be simplified using the conditional probability rule:

$$P(\Theta) = P(z|N, \Gamma)P(N)P(\Gamma)$$

As much as possible, weak assumptions should be made to write a robust prior then often flat priors (i.e., $P \propto$ const) are used. Priors should also be based on a physical meaning and not contradict the physical and observed properties of the objects. For the purpose of this model, the prior on N is assumed to be flat and the prior on the spectral index is a truncated Gaussian $P(\Gamma) \propto \mathcal{N}_G(\Gamma, \Gamma_{\rm Fermi}, \sigma_\Gamma)$ if $\Gamma < \Gamma_{\rm Fermi}$ and $P(\Gamma) = \propto$ const otherwise. The values of $\Gamma_{\rm Fermi}$ and σ_Γ are obtained by analyzing LAT data below 80 GeV (see Section 3 and Table 3). Here, it is assumed that the intrinsic spectrum in the VHE range cannot be harder than the *Fermi*-

LAT measurement. σ_Γ takes into account the statistical and systematic uncertainties on the *Fermi*-LAT measurement and also the systematic uncertainty on the H.E.S.S. spectrum ($\sigma = 0.20$, see Aharonian et al. 2006b) added quadratically and $\sigma_\Gamma = 0.33$ for a mean value of $\Gamma_{\rm Fermi} = 1.72$.

The prior on z is much more difficult to determine. A flat prior has no physical motivations since the probability to detect sources at TeV energy decreases with the redshift. The number of sources detected at TeV energy is not sufficient to use the corresponding redshift distribution as a prior.

A prior which takes into account the EBL can be derived assuming a population of sources with a constant spatial density. In the small space element $4\pi z^2 dz$, the number of such sources scales $\propto z^2$. For any given luminosity, their flux (which scales with the probability to detect them) is scaled by $z^{-2}\exp(-\tau(z))$. Lacking a proper knowledge of the intrinsic luminosity function of VHE γ-ray blazars, a reasonable assumption on the detection probability of a blazar at any redshift is a scaling proportional to the flux for a given luminosity, i.e., $\propto z^{-2}\exp(-\tau(z))$. Putting everything together, the prior on the redshift reads $P(z|N, \Gamma) = P(z) \propto \exp(-\tau(z))$.

Finally, the prior we use for our analysis is:

$$P(\Theta) \propto \exp(-\tau(z))\mathcal{N}_G(\Gamma, 1.72, 0.33) \quad \text{(A.1)}$$

if $\Gamma < 1.72$ and

$$P(\Theta) \propto \exp(-\tau(z))$$

otherwise. Putting all the components of the model together and marginalizing over the nuisance parameters N and Γ, the probability on the redshift can be computed numerically. The obtained mean value is $z = 0.49 \pm 0.04$. At a confidence level of 95%, the redshift is between $0.41 < z < 0.56$.

In this work, only the model of Franceschini et al. (2008) has been used. Other EBL models available in the literature predict slightly different absorption depths. This will lead to a small difference in the redshift. The use of a flat prior for the redshift distribution of the sources or a prior based on estimates of the HBLs luminosity function (Ajello et al. 2014) leads to changes of order of 0.01 on the resulting redshift.

APPENDIX B
DEVELOPMENT OF THE LIV METHOD

B.1 Modified Maximum Likelihood Method

In previous LIV studies with AGN flares (Albert et al. 2008; Abramowski et al. 2011) the signal was clearly dominating over the background, whereas in the present study the signal-over-background ratio is about 2. The background has been included in the formulation of the PDF: in the most general case, for given numbers of signal and background events s and b in the observation region ("ON" region), for a given dispersion parameter τ_n, the unbinned likelihood is:

$$L(n_{\rm ON}, n_{\rm OFF}|s, b, \tau_n) = {\rm Pois}(n_{\rm ON}|s+b)\cdot{\rm Pois}\left(n_{\rm OFF}\left|\frac{b}{\alpha}\right.\right) \cdot \prod_{i=1}^{n_{\rm ON}} P(E_i, t_i|s, b, \tau_n) \quad \text{(B.1)}$$

The PDF $P(E_i, t_i|s, b, \tau_n)$ associated with each gamma-like particle characterized by its time t_i and energy E_i contains two terms (signal and background):

$$P(E_i, t_i|s, b, \tau_n) = w_s \cdot P_{\rm Sig}(E_i, t_i|\tau_n) + (1 - w_s)\cdot P_{\rm Bkg}(E_i, t_i) \quad \text{(B.2)}$$

with

$$w_s = \frac{s}{s+b}. \quad \text{(B.3)}$$

$n_{\rm ON}$ is the number of events detected in the source ON region included in the fit range $[E_{\rm cut}; E_{\rm max}] \times [t_{\rm min}; t_{\rm max}]$. $n_{\rm OFF}$ is the number of events in the OFF regions, in the same (E, t) range; α is the inverse number of OFF regions. ${\rm Pois}(n_{\rm ON}|s+b)$ (${\rm Pois}(n_{\rm OFF}|b/\alpha)$) is the Poisson distribution with index $n_{\rm ON}$ ($n_{\rm OFF}$) and parameter $s + b$ (b/α). The likelihood function can be simplified by fixing s and b from a comparison of ON and OFF sets: $s = n_{\rm ON} - \alpha n_{\rm OFF}$ and $b = \alpha n_{\rm OFF}$. In this case, the Poisson terms in Equation (B.2) are equal to 1. The

Table B1
Selections Applied to the ON and OFF Data Sets

Selection	# of ON Events	Weighted # of OFF Events	S/B
Total sample	461 (100%)	144.3 (100%)	2.2
(1) = Time in 500–8500s	358 (77.7%)	95.8 (66.4%)	2.7
(1) and E in 0.3–0.789 TeV	154 (33.4%)	36.3 (25.1%)	3.2
(1) and E in 0.3–0.4 TeV (Template)	82 (17.8%)	14.2 (9.9%)	4.8
(1) and E in 0.4–0.789 TeV (LH fit)	72 (15.6%)	21.9 (15.2%)	2.3

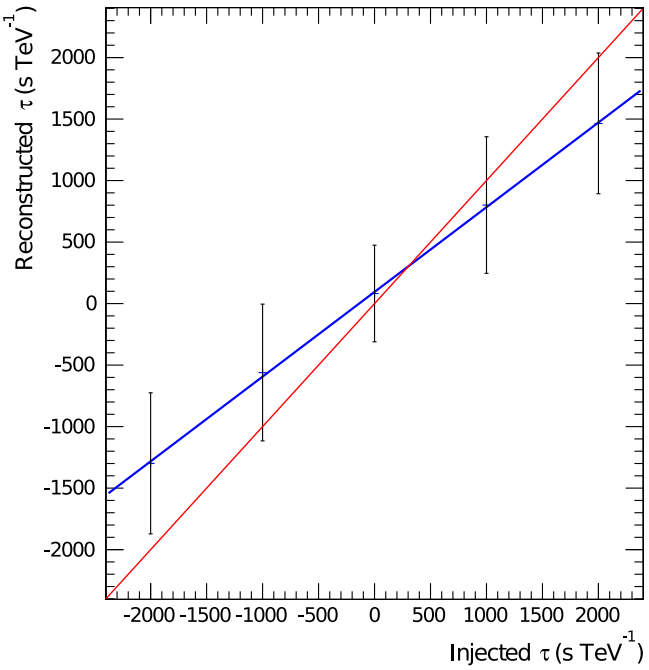

Figure B1. Means of the reconstructed dispersion vs. the real (injected dispersion) for the linear case $n = 1$; for a given injected dispersion, errors bars correspond to the means of the distribution of the upper and lower limits (90% 2-sided $\simeq$ 95% 1-sided). The blue line is a linear fit to the points. The red line shows the ideally obtained curve $\tau_{\rm reconstructed} = \tau_{\rm injected}$ obtained in the case S/B $= \infty$.

Table B2
Linear (Top) and Quadratic (Bottom) Dispersion Parameters; from left to right: Best Estimate, LL and UL from Data (Cut on Likelihood Curve), LL and UL from MC Simulations (means of Per-set LL and UL Distributions), Calibrated LL and UL (Combination of Data and MC), Calibrated LL and UL Including Systematic Errors

n	$\tau_{n,\mathrm{best}}^{\mathrm{data}}$	$\mathrm{LL}_n^{\mathrm{data}}$	$\mathrm{UL}_n^{\mathrm{data}}$	$\tau_{n,\mathrm{best}}^{\mathrm{MC}}$	$\mathrm{LL}_n^{\mathrm{MC}}$	$\mathrm{UL}_n^{\mathrm{MC}}$	$\mathrm{LL}_n^{\mathrm{calib}}$	$\mathrm{UL}_n^{\mathrm{calib}}$	$\mathrm{LL}_n^{\mathrm{calib}}$	$\mathrm{UL}_n^{\mathrm{calib}}$
									With Systematics	
1	−131.7	−806.7	554.7	99.1	−526.3	725.6	−757.1	494.8	−838.9	576.4
2	−287.5	−1449.9	853.6	217.2	−942.0	1395.0	−1446.7	890.3	−1570.5	1012.4

Note. Dispersion Parameters $\tau_{n,\mathrm{best}}$, LLs and ULs are in s TeV^{-n}.

probabilities P_{Sig} and P_{Bkg} are defined as:

$$P_{\mathrm{Sig}}(E_i, t_i|\tau_n) = \frac{1}{N(\tau_n)} \cdot R_{\mathrm{Sig}}(E_i, t_i|\tau_n) \quad \text{(B.4)}$$

$$P_{\mathrm{Bkg}}(E_i, t_i) = \frac{1}{N'} \cdot R_{\mathrm{Bkg}}(E_i, t_i) \quad \text{(B.5)}$$

with

$$R_{\mathrm{Sig}}(E, t|\tau_n) = \int_{E_{\mathrm{true}}=0}^{\infty} D(E, E_{\mathrm{true}}) A_{\mathrm{eff}}(E_{\mathrm{true}}, t) \times \Lambda_{\mathrm{Sig}}(E_{\mathrm{true}}) F_{\mathrm{Sig}}(t - \tau_n \cdot E_{\mathrm{true}}^n) dE_{\mathrm{true}} \quad \text{(B.6)}$$

$$R_{\mathrm{Bkg}}(E, t) = \int_{E_{\mathrm{true}}=0}^{\infty} D(E, E_{\mathrm{true}}) \times A_{\mathrm{eff}}(E_{\mathrm{true}}, t) \Lambda_{\mathrm{Bkg}}(E_{\mathrm{true}}) F_{\mathrm{Bkg}}(t) dE_{\mathrm{true}}. \quad \text{(B.7)}$$

$P_{\mathrm{Sig}}(E_i, t_i|\tau_n)$ is the probability that the event (E_i, t_i) is a photon emitted at the source and detected on Earth with a delay $\tau_n E^n$. It takes into account the emission (time distribution $F_{\mathrm{Sig}}(t)$ and energy spectrum $\Lambda_{\mathrm{Sig}}(E)$ at the source), the propagation (delay $\tau_n \cdot E_i^n$ due to possible LIV effect) and the detection of a photon by the detector (H.E.S.S. energy resolution $D(E, E_{\mathrm{true}})$ and effective area $A_{\mathrm{eff}}(E, t)$). $P_{\mathrm{Bkg}}(E_i, t_i)$ is the probability that the event (E_i, t_i) is a background event; it is not expected to be variable with time, thus $F_{\mathrm{Bkg}}(t)$ is a uniform time distribution: $F_{\mathrm{Bkg}}(t) = F_{\mathrm{Bkg}}$. The background energy distribution Λ_{Bkg} is measured from OFF regions. $N(\tau_n)$ (resp. N') is the normalization factor of the PDF P_{Sig} (resp. P_{Bkg}) in the range $[E_{\mathrm{cut}}; E_{\mathrm{max}}] \times [t_{\mathrm{min}}; t_{\mathrm{max}}]$ where the likelihood fit is performed.

Also, the energy resolution $D(E, E_{\mathrm{true}})$ is assumed to be perfect in the range $[E_{\mathrm{cut}}; E_{\mathrm{max}}]$.[53] This leads to simplified expressions of $P_{\mathrm{Sig}}(E_i, t_i|\tau_n)$ and $P_{\mathrm{Bkg}}(E_i, t_i)$:

$$P_{\mathrm{Sig}}(E_i, t_i|\tau_n) = \frac{1}{N(\tau_n)} \cdot A_{\mathrm{eff}}(E_i, t_i) \times \Lambda_{\mathrm{Sig}}(E_i) F_{\mathrm{Sig}}(t_i - \tau_n \cdot E_i^n) \quad \text{(B.8)}$$

$$P_{\mathrm{Bkg}}(E_i, t_i) = \frac{1}{N'} \cdot A_{\mathrm{eff}}(E_i, t_i) \Lambda_{\mathrm{Bkg}}(E_i) F_{\mathrm{Bkg}} \quad \text{(B.9)}$$

The best estimate of the dispersion parameter $\hat{\tau}_n$ is obtained by maximizing the likelihood $L(\tau_n)$.

[53] The actual energy resolution is of the order of 10% in this range.

B.2 Selection Cuts

Table B1 shows the effect of the selection cuts on the number of ON and OFF events. Other choices of E_{min} and E_{cut} did not introduce significant changes in the final results.

B.3 Test of the Method, CIs

The method has been tested on MC simulated sets. Each set was composed of $n_{\mathrm{ON}} = 72$ ON events, as in the real data sample:

1. $s = 50$ signal events with times following the template light curve (Figure 6) shifted by a factor $\tau_{n,\mathrm{inj}} \cdot E_i$; energies follow a power law spectrum of photon index $\Gamma_{\mathrm{Sig}} = 4.8$, degraded by the acceptance and convolved with the energy resolution.
2. $b = 22$ background events with times following a uniform distribution and energies drawn from a power law spectrum of index $\Gamma_{\mathrm{Bkg}} = 2.5$, degraded by the acceptance and convolvted with the energy resolution.

For a given injected dispersion, the maximum likelihood method is applied to each MC-simulated set. The initial light curve and energy spectrum were used as templates in the model instead of fitting them for each set.

Figure B1 shows the means of the reconstructed dispersion versus the real (injected) dispersion for $n = 1$; for a given injected dispersion, error bars correspond to the rms of the distribution of the best estimates $\hat{\tau}_1$. The blue line shows the result of a linear fit. The slope roughly corresponds to the percentage of signal in the total ON data set. It is due to the loss of sensitivity resulting from the part of the data sets with no dispersion. A systematic shift is observed of about 100 s TeV^{-1}, well bellow 1σ value—the rms of the best estimate distribution is 361 s TeV^{-1}. The results in this paper have not been corrected for this bias.

The coverage is not necessarily proper, i.e. the number of sets for which the injected dispersion value τ_{inj} lies between the set's LL and UL does not match the required 95% 1-sided confidence level. The common cut used on the likelihood curves to get the LLs/ULs has been iteratively adjusted to ensure a correct statistical coverage: using this new cut, 95% of the realizations provide CIs that include the injected dispersion $\tau_{n,\mathrm{inj}}$. The initial coverage was about 85% for a cut on $2 \ln L$ of 2.71. The new common cut, found iteratively at 3.5, ensures the desired 90% 2-sided CL (approx. 95% one-sided CL). Figure B2 shows the distributions of the best estimates, the 95% 1-sided LLs and ULs for $\tau_{1,\mathrm{inj}} = 0$ s TeV^{-1} (linear case) and $\tau_{2,\mathrm{inj}} = 0$ s TeV^{-2} (quadratic case); the means of the lower and upper limit distributions, shown as a

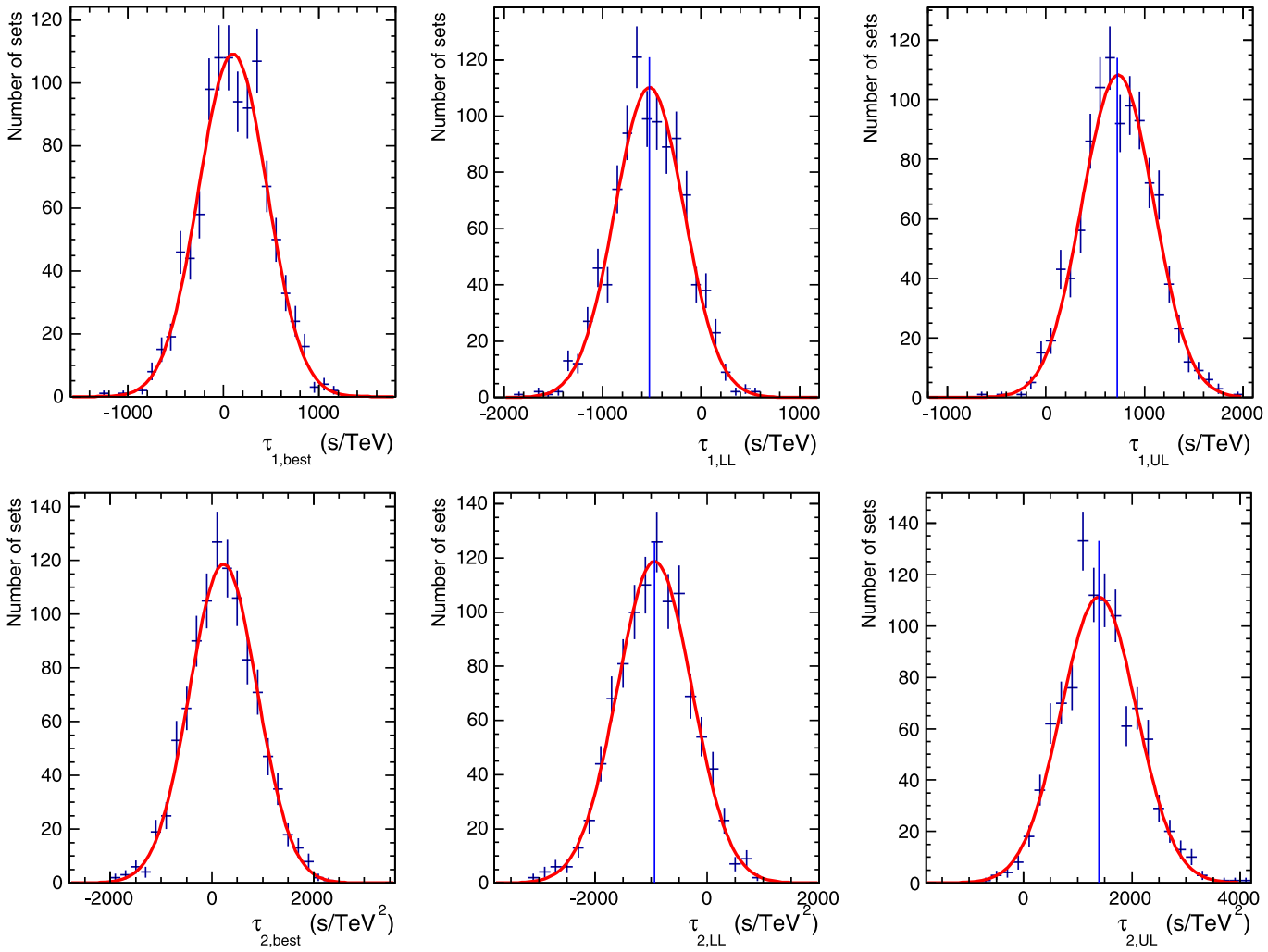

Figure B2. Distributions of the best estimates, the 95% one-sided lower and upper limits from simulations in case of no injected dispersion ($\tau_{n,\mathrm{inj}} = 0$ s TeV^{-n}), for $n = 1$ (top) and $n = 2$ (bottom); dispersion values are in s TeV^{-n}. The blue vertical line on the LL (resp. UL) distribution shows LL$^{\mathrm{MC}}$ (resp. UL$^{\mathrm{MC}}$), defined as the mean of the distribution.

blue vertical line, are used to construct the "calibrated confidence interval."

To get CIs from data, a maximum likelihood method is applied to the original data set and gives a best estimate $\tau_{\mathrm{best}}^{\mathrm{data}}$. The cut value determined from the simulations to ensure proper coverage is applied on the original data set to obtain LL$^{\mathrm{data}}$ and UL$^{\mathrm{data}}$. The "calibrated" limits LL$^{\mathrm{calib}}$ and UL$^{\mathrm{calib}}$, combining $\tau_{\mathrm{best}}^{\mathrm{data}}$ from data together with MC results, are taken as

$$\begin{aligned} \mathrm{LL}^{\mathrm{calib}} &= \tau_{\mathrm{best}}^{\mathrm{data}} - |\tau_{\mathrm{best}}^{\mathrm{MC}} - \mathrm{LL}^{\mathrm{MC}}| \\ \mathrm{UL}^{\mathrm{calib}} &= \tau_{\mathrm{best}}^{\mathrm{data}} + |\tau_{\mathrm{best}}^{\mathrm{MC}} - \mathrm{UL}^{\mathrm{MC}}| \end{aligned} \qquad \text{(B.10)}$$

with $\tau_{\mathrm{best}}^{\mathrm{MC}}$, LL$^{\mathrm{MC}}$ and UL$^{\mathrm{MC}}$ defined as the means of the per-set best-estimate distribution, LL distribution, and UL distribution respectively.

Table B2 lists the CIs determined in both ways, i.e., data-only and calibrated ones: $\mathrm{LL}_n^{\mathrm{data}}$ and $\mathrm{LL}_n^{\mathrm{calib}}$ (resp. $\mathrm{UL}_n^{\mathrm{data}}$ and $\mathrm{UL}_n^{\mathrm{calib}}$) are compatible within 10%. In this work, calibrated CIs have been used to derive the final LLs on E_{QG}. They are preferred over data-only CIs as they provide statistically well defined confidence levels. They also ensure coherent comparison with previous published results, e.g., with PKS 2155-304 by Abramowski et al. (2011) and GRB studies by Vasileiou et al. (2013).

Table B3
Summary of all Studied Systematic Contributions. The Main Systematic Errors are due to the Uncertainties on the Light Curve Parametrization

	Estimated Error on Input Parameters	τ_1 (s TeV^{-1})	τ_2 (s TeV^{-2})
Background contribution	···	<45	<80
Acceptance factors	10%	<1	<1
Energy resolution	10%	<55	<85
Photon index	5%	<55	<50
Light curve parameterization	···	<300	<500
Systematic bias	···	~100	~200
Total: $\sqrt{\sum_i \mathrm{syst}_i^2}$		<330	<555

B.4 Estimation of the Systematics

Estimations of the systematic effects on the dispersion measurement were performed. It was found that the main

systematic errors are due to the uncertainties on the light curve parameterization. Other sources of systematic errors include the contribution of the background, effect of the change of photon index, the energy resolution and the effective area determination of the detector. To study the following four contributions, new simulated data sets have been built, each one with different input parameters:

1. background contribution: photons and background events have been reallocated within the ON data set in the fit range $[E_{\rm cut}; E_{\rm max}]$, introducing a 1σ fluctuation in the number of signal event s in the ON data set;
2. effective area: set to a constant, equal to 120000 m^2 for all energies and all times, which corresponds to a maximum shift of 10% (the actual effective area increases with energy);
3. energy resolution: reconstructed energies have been replaced by the true energies; this corresponds to a shift of about 10% on the reconstructed energy values;
4. photon index: changed by one standard deviation (± 0.25).

For the determination of systematic errors arising from the light curve parameterization, the calibration of the CIs has been redone using successively the upper 1σ and the lower 1σ contours of the template, shown in Figure 6. The change in mean lower and ULs on the dispersion parameter τ_n gives an estimate of the systematic error associated to each contribution.[54] An additional systematic contribution comes from the shift arising from the method found with simulation (see Appendix B.3). Table B3 summarizes all studied systematic contributions. The overall estimated systematic error on τ_n is 330 s TeV^{-1} for the linear case ($n = 1$) and 555 s TeV^{-2} for the quadratic case ($n = 2$); they were included in the calculation of the limits on $E_{\rm QG}$ by adding the statistical and the systematic errors in quadrature.

REFERENCES

Abdo, A. A., Ackermann, M., Ajello, M., et al. 2009a, ApJ, 707, 1310
Abdo, A. A., Ackermann, M., Ajello, M., et al. 2009b, ApJS, 183, 46
Abdo, A. A., Ackermann, M., Ajello, M., et al. 2010a, ApJ, 708, 1310
Abdo, A. A., Ackermann, M., Ajello, M., et al. 2010b, ApJ, 722, 520
Abramowski, A., Acero, F., Aharonian, F., et al. 2011, APh, 34, 738
Abramowski, A., Acero, F., Akhperjanian, A. G., et al. 2013a, A&A, 552, A118
Abramowski, A., Acero, F., Aharonian, F., et al. 2013b, A&A, 550, A4
Abramowski, A., Acero, F., Aharonian, F., et al. 2014, A&A, submitted
Ackermann, M., Ajello, M., Albert, A., et al. 2012a, ApJS, 203, 4
Ackermann, M., Ajello, M., Allafort, A., et al. 2012b, Sci, 338, 1190
Aharonian, F., Akhperjanian, A. G., Bazer-Bachi, A. R., et al. 2006a, A&A, 448, L19
Aharonian, F., Akhperjanian, A. G., Bazer-Bachi, A. R., et al. 2006b, A&A, 457, 899
Aharonian, F., Akhperjanian, A. G., Bazer-Bachi, A. R., et al. 2007a, ApJL, 664, L71
Aharonian, F., Akhperjanian, A. G., Bazer-Bachi, A. R., et al. 2007b, ApJL, 664, L71
Aharonian, F., Akhperjanian, A. G., Barres de Almeida, U., et al. 2008, A&A, 477, 481
Ajello, M., Romani, R. W., Gasparrini, D., et al. 2014, ApJ, 780, 73
Albert, J., Aliu, E., Anderhub, H., et al. 2008, PhLB, 668, 253
Aleksić, J., Alvarez, E. A., Antonelli, L. A., et al. 2012, ApJ, 748, 46
Aleksić, J., Ansoldi, S., Antonelli, L. A., et al. 2014, arXiv:1408.1975
Aliu, E., Archer, A., Aune, T., et al. 2015, ApJ, 799, 7
Atwood, W. B., Abdo, A. A., Ackermann, M., et al. 2009, ApJ, 697, 1071
Becherini, Y., Djannati-Ataï, A., Marandon, V., Punch, M., & Pita, S. 2011, APh, 34, 858
Berge, D., Funk, S., & Hinton, J. 2007, A&A, 466, 1219
Biller, S. D., Breslin, A. C., Buckley, J., et al. 1999, PhRvL, 83, 2108
Bregeon, J., Charles, E., & Wood, M. for the Fermi-LAT collaboration 2013, arXiv:1304.5456
Cortina, J. 2012a, ATel, 3977, 1
Cortina, J. 2012b, ATel, 4069, 1
Danforth, C. W., Keeney, B. A., Stocke, J. T., Shull, J. M., & Yao, Y. 2010, ApJ, 720, 976
de Naurois, M., & Rolland, L. 2009, APh, 32, 231
Franceschini, A., Rodighiero, G., & Vaccari, M. 2008, A&A, 487, 837
Gaidos, J. A., Akerlof, C. W., Biller, S. D., et al. 1996, Natur, 383, 319
Giommi, P., Ansari, S. G., & Micol, A. 1995, A&AS, 109, 267
Green, R. F., Schmidt, M., & Liebert, J. 1986, ApJS, 61, 305
Hauser, M. G., & Dwek, E. 2001, ARA&A, 39, 249
Hinton, J. A. The H.E.S.S. Collaboration 2004, NewAR, 48, 331
Jacob, U., & Piran, T. 2008, J. Cosmol. Astropart. Phys., 2008, 031
Komatsu, E., Smith, K. M., Dunkley, J., et al. 2011, ApJS, 192, 18
Li, T.-P., & Ma, Y.-Q. 1983, ApJ, 272, 317
Liberati, S. 2013, CQGra, 30, 133001
Martinez, M., & Errando, M. 2009, APh, 31, 226
Mattingly, D. 2005, LRR 8
Mattox, J. R., Bertsch, D. L., Chiang, J., et al. 1996, ApJ, 461, 396
Osterman, M. A., Miller, H. R., Campbell, A. M., et al. 2006, AJ, 132, 873
Piron, F., Djannati-Atai, A., Punch, M., et al. 2001, A&A, 374, 895
Prandini, E., Dorner, D., Mankuzhiyil, N., et al. 2009, arXiv: 0907.0157
Rector, T. A., Gabuzda, D. C., & Stocke, J. T. 2003, AJ, 125, 1060
Reimer, A., Costamante, L., Madejski, G., Reimer, O., & Dorner, D. 2008, ApJ, 682, 775
Sanchez, D. A., & Deil, C. 2013, arXiv:1307.4534
Sanchez, D. A., Fegan, S., & Giebels, B. 2013, A&A, 554, A75
Scargle, J. D. 1998, ApJ, 504, 405
Sol, H., Zech, A., Boisson, C., et al. 2013, APh, 43, 215
Treves, A., Falomo, R., & Uslenghi, M. 2007, A&A, 473, L17
Urry, C. M., & Padovani, P. 1995, PASP, 107, 803
Vasileiou, V., Jacholkowska, A., Piron, F., et al. 2013, PhRvD, 87, 122001
Vaughan, S., Edelson, R., Warwick, R. S., & Uttley, P. 2003, MNRAS, 345, 1271

[54] In particular the errors on the peak positions constitute the most important part of the uncertainty on the template light curve contributing to the likelihood fit—see previous works, e.g., Abramowski et al. (2011). Therefore, the covariance matrix of the fit of the template was studied in detail; the peak positions were varied by values of $\pm 1\sigma$ extracted from the covariance matrix. This study led to an increase in overall systematics of the order of 20% for τ_1 and 40% for τ_2, and a decrease of maximum 7% and 2% of limits on $E_{\rm QG,1}$ and $E_{\rm QG,2}$ respectively.